Noninvasive Determination of 2-[18F]-Fluoroisonicotinic Acid Hydrazide Pharmacokinetics by Positron Emission Tomography in Mycobacterium tuberculosis-Infected Mice

Antimicrobial Agents and Chemotherapy

Noninvasive Determination of 2-[^{18}F]-Fluoroisonicotinic Acid Hydrazide Pharmacokinetics by Positron Emission Tomography in Mycobacterium tuberculosis-Infected Mice

E. A. Weinstein, L. Liu, A. A. Ordonez, H. Wang, J. M. Hooker, P. J. Tonge and S. K. Jain

Antimicrob. Agents Chemother. **2012, 56(12):6284. DOI: 10.1128/AAC.01644-12.**
Published Ahead of Print 24 September 2012.

AAC Journals.ASM.org

Noninvasive Determination of 2-[^{18}F]-Fluoroisonicotinic Acid Hydrazide Pharmacokinetics by Positron Emission Tomography in *Mycobacterium tuberculosis*-Infected Mice

E. A. Weinstein,[a,b,c] L. Liu,[d] A. A. Ordonez,[a,b,e] H. Wang,[d] J. M. Hooker,[f] P. J. Tonge,[d] and S. K. Jain[a,b,e]

Center for Infection and Inflammation Imaging,[a] Center for Tuberculosis Research,[b] Department of Medicine,[c] and Department of Pediatrics,[e] Johns Hopkins University School of Medicine, Baltimore, Maryland, USA; Institute for Chemical Biology & Drug Discovery, Department of Chemistry, Stony Brook University, Stony Brook, New York, USA[d]; and Martinos Center for Biomedical Imaging, Massachusetts General Hospital and Harvard Medical School, Charlestown, Massachusetts, USA[f]

Tuberculosis (TB) is a global pandemic requiring sustained therapy to facilitate curing and to prevent the emergence of drug resistance. There are few adequate tools to evaluate drug dynamics within infected tissues *in vivo*. In this report, we evaluated a fluorinated analog of isoniazid (INH), 2-[^{18}F]fluoroisonicotinic acid hydrazide (2-[^{18}F]-INH), as a probe for imaging *Mycobacterium tuberculosis*-infected mice by dynamic positron emission tomography (PET). We developed a tail vein catheter system to safely deliver drugs to *M. tuberculosis* aerosol-infected mice inside sealed biocontainment devices. Imaging was rapid and noninvasive, and it could simultaneously visualize multiple tissues. Dynamic PET imaging demonstrated that 2-[^{18}F]-INH was extensively distributed and rapidly accumulated at the sites of infection, including necrotic pulmonary TB lesions. Compared to uninfected animals, *M. tuberculosis*-infected mice had a significantly higher PET signal within the lungs ($P < 0.05$) despite similar PET activity in the liver ($P > 0.85$), suggesting that 2-[^{18}F]-INH accumulated at the site of the pulmonary infection. Furthermore, our data indicated that similar to INH, 2-[^{18}F]-INH required specific activation and accumulated within the bacterium. Pathogen-specific metabolism makes positron-emitting INH analogs attractive candidates for development into imaging probes with the potential to both detect bacteria and yield pharmacokinetic data *in situ*. Since PET imaging is currently used clinically, this approach could be translated from preclinical studies to use in humans.

The importance of sustained, adequate antimicrobial therapy is highlighted by *Mycobacterium tuberculosis*, which is causing a surging global epidemic with an estimated 8.8 million new patients with active disease and 1.5 million deaths annually (41). Many of the 2.2 billion people latently infected with *M. tuberculosis* develop reactivation disease, sometimes decades after the initial infection (19). Coinfection with human immunodeficiency virus (HIV) increases the risk of relapse from a lifetime risk of 5 to 10% to approximately 10% per year (10).

Tuberculosis (TB) is typically treated with 6 months of combination therapy using isoniazid (INH) as a primary agent due to its remarkable sterilizing activity against actively dividing bacilli (9, 10). The treatment regimen was developed using serum pharmacokinetic (PK) values and historic measures of efficacy (5, 16). Nevertheless, a growing number of studies support the importance of monitoring drug concentration in infected tissues (17, 26), and current Food and Drug Administration (FDA) guidelines require tissue drug distribution studies at infected and uninfected sites (26). Serious consequences of inadequate drug concentration in target tissues include treatment failure and selection pressure for antibiotic-resistant organisms (31). Conversely, in severely ill patients, normal physiology may be compromised, thus elevating the risk of renal and hepatic toxicity (24).

INH is a prodrug with complex bacterial metabolism. Consensus holds that it is first oxidized by the mycobacterial catalase-peroxidase enzyme KatG and then conjugates with NAD (39, 42) to form an INH-NAD adduct that inhibits the enoyl-acyl carrier protein (enoyl-ACP) reductase InhA, among other targets (3, 27, 34, 39, 42). INH is hypothesized to accumulate within the mycobacterium as trapped metabolites, including the INH-NAD adduct, which dissociates slowly from InhA (22, 33). To evaluate this hypothesis and explore the potential of INH as a reporter of bacterial localization *in vivo*, a method is needed that can report on drug concentration at the site of infection. New techniques, such as matrix-assisted laser desorption ionization (MALDI) mass spectrometry, have the power to detect drugs and their metabolites within a granuloma (32) but are invasive and rely on accurate resection of tissue. Positron emission tomography (PET) is a noninvasive alternative to determine the characteristics of drug absorption, distribution, and elimination in both clinical and preclinical settings (8, 12, 20). The pathogen-specific metabolism and accumulation of INH makes it an attractive imaging probe with the potential to both detect bacteria and yield PK data *in situ* (15). We recently reported the bioimaging of [^{11}C]-INH and two other carbon-11-labeled TB therapeutics in healthy baboons (20). We have now extended this work to the evaluation of a fluorine-18 analog of INH, which also has the advantage of translation to clinical settings (25). Furthermore, we have progressed from healthy control animals to imaging animals with active *M. tuberculosis* infections. To accomplish this safely, we developed and utilized a novel on-table injection system to noninvasively deter-

Received 9 August 2012 **Returned for modification** 28 August 2012
Accepted 17 September 2012
Published ahead of print 24 September 2012
Address correspondence to Sanjay K. Jain, sjain5@jhmi.edu.
E.A.W. and L.L. contributed equally.

doi:10.1128/AAC.01644-12

mine a multitissue host pharmacokinetic profile of 2-[^{18}F]-INH in *M. tuberculosis*-infected mice.

MATERIALS AND METHODS

The chemicals used in the study all were purchased from commercial vendors and were used without further purification except where stated. ^{18}F was purchased from PETNET Solutions Inc. (Philadelphia, PA) on ion-exchange resin. Chemical and radiochemical purities were determined by thin-layer chromatography (TLC) and an analytical high-performance liquid chromatography (HPLC) system equipped with both UV and radioactivity detectors. The purities of the intermediate and final products were >95%.

Synthesis of 2-F-INH and 2-[^{18}F]-INH. The syntheses of 2-fluoroisonicotinic acid hydrazide (2-F-INH) and 2-[^{18}F]fluoro-isonicotinic acid hydrazide (2-[^{18}F]-INH) were performed from 2-fluoropyridine-4-carboxylic acid as described previously (2, 35) (see Fig. S1 in the supplemental material for details). Radiochemical purity was determined by reverse-phase analytical high-performance liquid chromatography (HPLC) (PFP; 250 by 4.6, 5-μm column; Phenomenex) using a mobile phase of 5% MeCN–95% H_2O and confirmed by TLC (10% MeOH–90% CH_2Cl_2) cospotting of the labeled product with a standard.

Inactivation of InhA by INH or 2-F-INH. The *M. tuberculosis* enoyl-ACP reductase (InhA) was expressed and purified as previously described (23), and catalase peroxidase (KatG) was provided as a gift from Richard Magliozzo (Department of Chemistry, Brooklyn College, NY). *Trans*-2-dodecenoyl-coenzyme A (DD-CoA) was synthesized from *trans*-dodecenoic acid as previously described (29). InhA (0.5 μM) was incubated with 0.5 μM KatG, 50 μM NAD^+, 50 μM INH (or F-INH), and 2 mM EDTA in a total volume of 1.0 ml at 25°C in buffer [30 mM piperazine-*N*,*N*′-bis(2-ethanesulfonic acid), 150 mM NaCl, pH 6.8]. Aliquots were taken at 5, 10, 20, 30, 40, 50, 60, 90, and 120 min, and then DD-CoA (20 μM) and NADH (250 μM) were added. InhA activity was measured by following the oxidation of NADH to NAD^+ at 340 nm in a Cary 100 Bio spectrophotometer (Varian). InhA activity was expressed as a percentage of the value measured at time zero (43). Three independent replicates were used for each group.

***M. tuberculosis* strains and *in vitro* uptake assays.** Frozen stocks of wild-type *M. tuberculosis* H37Rv as well as previously validated *katG* W149R, *katG* M1A, and *inhA* T(−8) INH-resistant strains in the *M. tuberculosis* H37Rv background (1) were grown to mid-log phase in Middlebrook 7H9 broth supplemented with 10% oleic acid-albumin-dextrose-catalase (Difco, Detroit, MI) and 0.05% Tween 80 (Sigma). MICs were determined for each strain with INH and 2-F-INH by the broth macrodilution method (National Committee for Clinical Laboratory Standard M07-A8). 2-[^{18}F]-INH uptake assays were performed by incubating bacterial cultures with 0.148 MBq per ml of 2-[^{18}F]-INH at 37°C with rapid agitation for 8 h. Heat-killed (90°C for 20 min) controls for each bacterial strain were similarly incubated with 2-[^{18}F]-INH. Bacteria were pelleted by centrifugation and washed twice with phosphate-buffered saline (PBS). All live bacterial cultures were heat inactivated prior to measurements. The activity for each pellet was measured using an automated gamma counter (1282 Compugamma CS Universal gamma counter; LKB Wallac). Background counts were subtracted from sample counts. Five independent replicates were used for each sample.

Murine *M. tuberculosis* model (*in vivo* aerosol infection). Five- to 6-week-old female BALB/c (Charles River) or C3HeB/FeJ (Jackson Laboratory) mice were aerosol infected with log-phase broth cultures of *M. tuberculosis* H37Rv using the Middlebrook inhalation exposure system (Glas-Col). Mice were sacrificed the day after infection to determine the number of bacilli implanted in the lungs and also at the time of imaging. The entire lungs were homogenized in phosphate-buffered saline and plated onto Middlebrook 7H11 selective plates (Becton, Dickinson). At least 3 mice were used for each time point. All plates were incubated at 37°C for 4 weeks before the CFU were determined. A separate group of identically infected mice were used for imaging studies.

On-table injection system. A 30-gauge needle (BD Bioscience), attached to polyethylene-10 tubing (Braintree Scientific), was inserted into the lateral tail vein of anesthetized *M. tuberculosis*-infected mice as a catheter for on-table tracer delivery (see Fig. S2 in the supplemental material). The live animals were then placed inside sealed biocontainment devices as described before (7, 8), with the polyethylene-10 tubing extending through one of the ports of the biocontainment device. The device was seal tested, and a 1-ml insulin syringe was attached to the catheter hub to deliver radiotracer at the beginning of imaging.

[^{18}F]FDG-PET and CT imaging. Mice were fasted for 12 h before each imaging time point. Water was provided *ad libitum*. On the day of imaging, each mouse was weighed, anesthetized, and then injected with (nominally) 7.4 MBq of [^{18}F]-fluorodeoxyglucose ([^{18}F]-FDG) via the tail vein and imaged 45 min postinjection using a Mosaic HP (Philips) small-animal PET imager using a single-frame, 15-min acquisition. A computed tomography (CT) scan was also performed at the same time using the NanoSPECT/CT (Bioscan) *in vivo* animal imager. PET images were reconstructed and coregistered with CT images. Three mice were used for each group. Amira version 5.4.2 (Amira) was used to visualize the images.

2-[^{18}F]-INH-PET/CT imaging. One week later, the same mice previously imaged by [^{18}F]-FDG were weighed, injected with (nominally) 7.4 MBq of 2-[^{18}F]-INH via the tail vein, and imaged. Since ^{18}F has a radioactive half-life of 109 min, it is completely decayed and does not interfere with the 2-[^{18}F]-INH imaging 1 week later. C3HeB/FeJ mice were imaged 20 min postinjection using the Mosaic HP (Philips) small-animal PET imagers with a dynamic (list mode) acquisition for 120 min. BALB/c mice were imaged immediately after tracer injection by utilizing the on-table injection system. List-mode data were framed as follows: 5 times for 2 min each, and then 10 times for 5 min each. Infected and uninfected controls were scanned two at a time as matched pairs, and data were obtained from 3 matched pairs (3 infected and 3 uninfected animals). CT scans were performed subsequent to PET imaging using the NanoSPECT/CT (Bioscan) *in vivo* animal imager. PET data were reconstructed and coregistered with CT images. Three mice were used for each group.

For semiquantitative analysis, 1 to 2 spherical (3-mm-diameter) regions of interest (ROI) were drawn manually using Amide version 0.9.1 (amide.sourceforge.net) in the lung, liver, and brain fields using CT as a guide. The standard uptake values (SUV) were computed by normalizing the ROI activity for each mouse to the injected dose and animal weight. For each group, the mean lung uptake of radioactivity at each time point was calculated by averaging the normalized lung SUV of all of the ROIs in that group. Amira was used to visualize the images.

All protocols were approved by the Johns Hopkins Biosafety, Radiation Safety, and Animal Care and Use Committees.

Statistical analysis. Statistical comparison between groups was performed using one-tail-distribution, two-sample, unequal-variance *t* tests in Excel 2007 (Microsoft). Data are presented on a linear scale as means ± standard errors for mean PET activities.

RESULTS

2-F-INH accumulates in *M. tuberculosis*. Respective MICs for 2-F-INH and INH were 8 and 0.025 μg/ml for the wild-type *M. tuberculosis*, >32 and >2 μg/ml for the *katG* promoter mutant (M1A), >32 and >1 μg/ml for the *katG* point mutant (W149R), and >32 and 0.1 μg/ml for the *inhA* promoter mutant [T(−8)]. Time-dependent inactivation of InhA by INH and 2-F-INH as measured by monitoring the oxidation of NADH *in vitro* is shown in Fig. 1A. Inactivation of InhA followed first-order kinetics for the first 60 min with a rate constant of 0.0299 and 0.0104 min^{-1} for INH and 2-F-INH, respectively. Complete inhibition of InhA was achieved within 90 min with INH, whereas 2-F-INH required over 120 min. In the control groups (without KatG), InhA was only minimally inhibited by either INH or 2-F-INH, confirming that both INH and 2-F-INH required KatG activation prior to

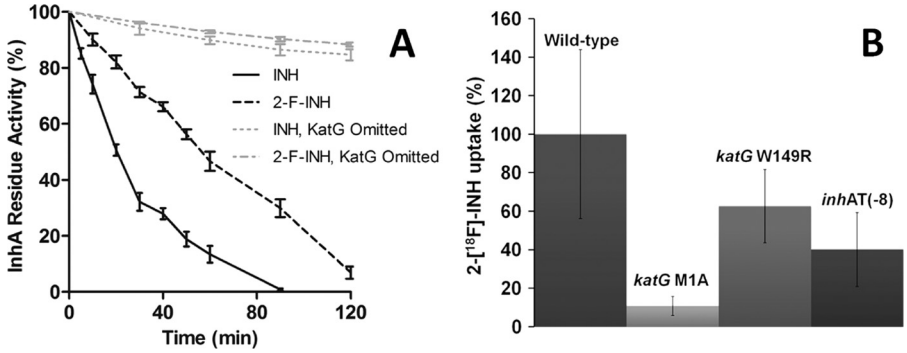

FIG 1 2-F-INH inhibits InhA and accumulates in *M. tuberculosis*. (A) The time-dependent inactivation of InhA by INH and 2-fluoroisonicotinic acid hydrazide (2-F-INH) was measured by monitoring the oxidation of NADH *in vitro*. Three independent replicates were used for each group. The InhA activity is expressed as a percentage of the activity measured at time zero. Complete inhibition of InhA was achieved within 90 min with INH, whereas 2-F-INH required about 120 min. In the control groups (omission of KatG), InhA is only minimally inhibited for both INH and 2-F-INH. (B) Intracellular accumulation of 2-[^{18}F]-INH in INH-resistant strains following an 8-h incubation is shown as a percentage of uptake compared to that of wild-type *M. tuberculosis*. Five independent replicates were used for each group. 2-[^{18}F]-INH readily accumulates within wild-type *M. tuberculosis*, and only the most INH-resistant strain (*katG* M1A) demonstrates significantly reduced intracellular accumulation. Taken together, these data indicate that although the addition of fluorine at the second position significantly decreases activity against InhA, 2-F-INH follows a pattern of metabolism and bacterial uptake similar to that of INH. Error bars represent the standard errors of the means.

InhA inhibition. Finally, we tested the intracellular accumulation of 2-[^{18}F]-INH in wild-type *M. tuberculosis* and INH-resistant strains (Fig. 1B). Following an 8-h incubation, 2-[^{18}F]-INH readily accumulated within wild-type *M. tuberculosis*. Only the most INH-resistant strain, *katG* M1A, demonstrated significantly reduced intracellular accumulation of 2-[^{18}F]-INH. No accumulation of 2-[^{18}F]-INH was noted in any of the heat-killed strains (data not shown). Taken together, these data indicate that although the 2-fluoro group significantly reduces the antibacterial activity of INH and decreases the ability of INH to inhibit InhA, 2-F-INH follows a pattern of metabolism and bacterial uptake similar to that of INH.

PET imaging of 2-[^{18}F]-INH in *M. tuberculosis*-infected mice. We hypothesized that the metabolism of INH by *M. tuberculosis* KatG results in selective intracellular trapping of INH and therefore generates a specific PET signal at the site of TB disease. 2-[^{18}F]-INH was synthesized and purified by a modified method of Amartey et al. (2) with resultant specific activity of 7.4 to 11.1 MBq/μmol at the time of delivery to the animal.

Aerosol-infected BALB/c mice were imaged 8 weeks postinfection, at which point there was diffuse pulmonary disease and $\log_{10}(6.4 \pm 0.3)$ CFU in the lungs. There was no significant difference in weight between the infected and uninfected animals. Coregistered [^{18}F]FDG-PET and CT images of a representative matched pair are shown in Fig. 2A. As expected, diffuse [^{18}F]FDG-PET activity was noted in the lung fields in infected animals but not in uninfected animals. Background uptake was noted in the heart, kidneys, and bladder of both the uninfected and infected animals. Coregistered 2-[^{18}F]-INH-PET/CT images from the same animals are shown in Fig. 2B. Diffuse PET activity was again noted in the lung fields in the infected animal but not the uninfected mouse. Background PET signal in the heart, liver, kidneys, and bladder was noted in both infected and uninfected animals.

Similar experiments were performed in C3HeB/FeJ mice for their intrinsic ability to form localized and well-defined TB lesions with central necrosis and hypoxia (13, 28). Mice were imaged 17 weeks after a low-dose aerosol infection, at which point there were well-defined pulmonary lesions and $\log_{10}(6.7 \pm 0.3)$ CFU in the lungs. Discrete foci of 2-[^{18}F]-INH-PET activity colocalizing with the TB lesions (as seen on CT) were noted in the lung fields of the infected mouse but not in the uninfected animal (Fig. 3), suggesting that 2-[^{18}F]-INH penetrated and concentrated at the site of TB lesions. As expected, and similar to that for BALB/c mice, uptake in the heart, liver, kidneys, and bladder was noted in both infected and uninfected animals.

Organ compartment pharmacokinetics of 2-[^{18}F]-INH. Given the qualitative differences in 2-[^{18}F]-INH-PET signal between *M. tuberculosis*-infected and uninfected mice, we performed additional quantitative analyses. Following simultaneous 2-[^{18}F]-INH injections into paired infected and uninfected BALB/c mice, we performed dynamic PET acquisitions over time. As shown in Fig. 4A, there was significantly more 2-[^{18}F]-INH-PET activity in the lung fields of infected mice than in uninfected controls from 40 min postinjection to the end of the recording at 60 min ($P < 0.05$). A signal-to-background ratio of 1.67 ± 0.04 was achieved from 40 to 60 min after tracer injection. Similarly, uptake of 2-[^{18}F]-INH was also evaluated in the brain. Probe uptake peaked 15 min postinjection and then slowly diffused away (Fig. 4B). While the signal was greater in infected mice, it was not statistically significant ($P > 0.50$). As expected, the liver intensities were not significantly different ($P > 0.85$) between the infected and uninfected animals (Fig. 4C) but they demonstrated high activity, as this is the site of INH metabolism. To extrapolate these data into a therapeutic context, an INH dose of 6.25 mg/kg of body weight in BALB/c mice produces a maximum concentration of drug in serum (C_{max}) of 4 μg/ml at 15 min (1). Using the heart as a proxy for the whole-blood concentration of 2-[^{18}F]-INH, the C_{max} in infected lung is calculated to be 3.5 μg/ml, and it is 3.3 μg/ml in uninfected controls. The differential uptake ratios of heart, lung, brain, liver, and kidney that correspond to the C_{max} (at the 15-min time point) are presented in Table S1 in the supplemental material.

DISCUSSION

INH has been the mainstay of TB treatment since its introduction in 1952 (6, 33). While the absorption from the gastrointestinal

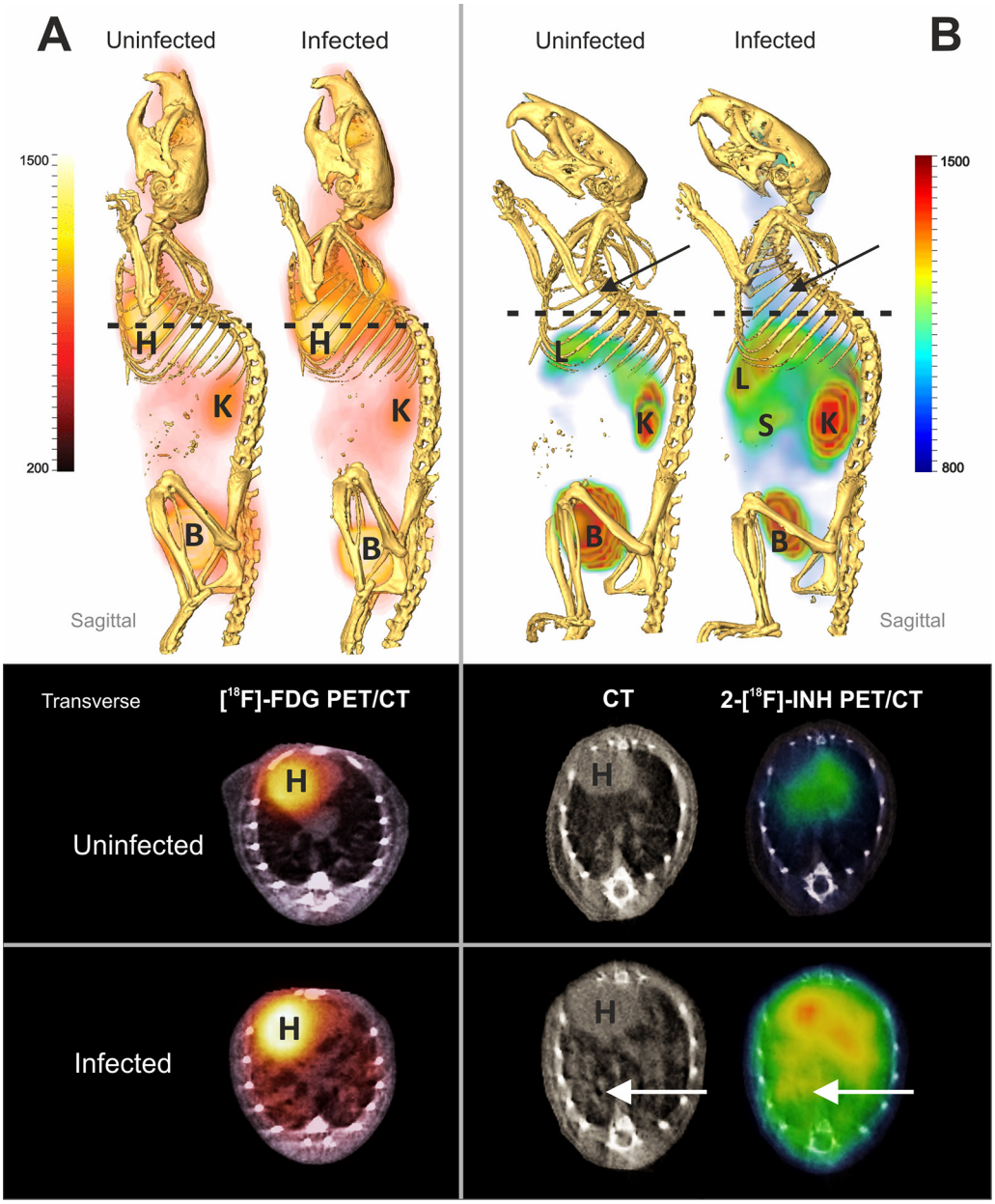

FIG 2 PET/CT imaging of *M. tuberculosis*-infected mice with diffuse pulmonary disease. Infected and uninfected BALB/c pairs were imaged after injection of 2-[^{18}F]-FDG (A) or 2-[^{18}F]-INH (B). Whole-animal sagittal and transverse sections are displayed as combined PET/CT images with heart (H), liver (L), kidneys (K), spleen (S), and bladder (B) marked. [^{18}F]FDG-PET activity is noted in the lung fields in infected animals but not uninfected animals (A). Background uptake is noted in the heart, kidneys, and bladder of both the uninfected and infected animals. Similarly, diffuse 2-[^{18}F]-INH-PET activity is noted in the lung fields of the infected animal but not the uninfected mouse (B). Background PET signal in the heart, liver, kidneys, and bladder is noted in both infected and uninfected animals.

tract is rapid and biodistribution nearly approaches that of water (20, 40), the elimination of drug depends on age and genetic factors, following a trimodal distribution in the general population (30, 36). The pharmacokinetic variability of INH metabolism is associated with treatment failure as well as acquired drug resistance (31). Indeed, drug levels were found to be subtherapeutic among patients with a slow response to TB therapy, suggesting that individualized dosing is more effective than standard dosing (14). Like most antimicrobial agents, INH requires transport to the site of infection and interaction with the pathogen. As a result, determining the drug concentration at the site of action is a more accurate approach to determining pharmacodynamic relationships than plasma drug concentration (4). Traditional pharmacokinetic methods involve the sacrifice and dissection of animals, which in itself alters tissue physiology. One solution to this dilemma has been the use of clinical microdialysis for continuous monitoring of drug bioavailability (37), but the technique requires precise anatomic knowledge of the lesion location for probe insertion. TB produces diverse lesions that are often difficult to localize (11). In the current study, we therefore utilized PET im-

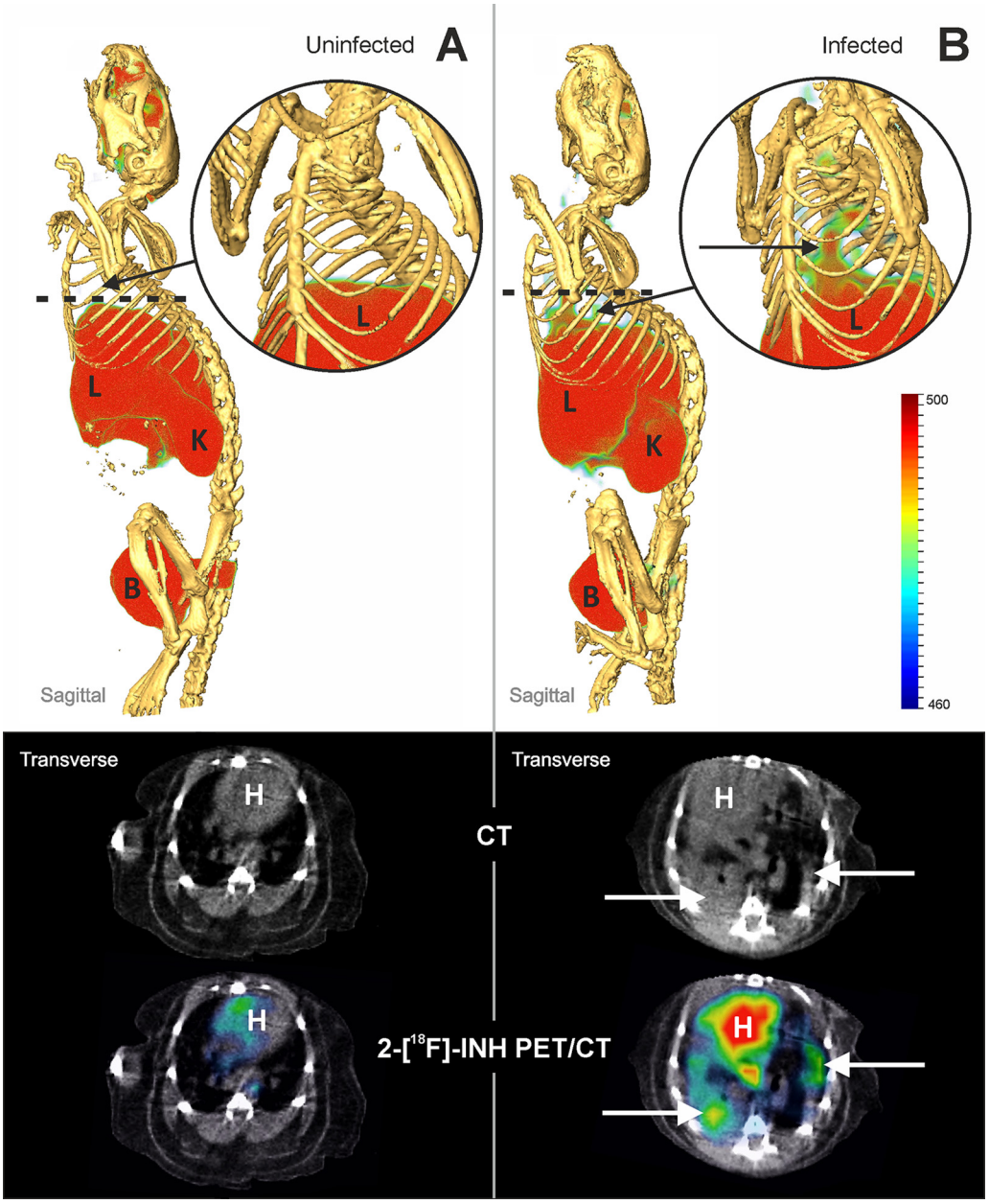

FIG 3 PET/CT imaging of *M. tuberculosis*-infected mice with discrete TB lesions, central necrosis, and hypoxia. Uninfected (A) and infected (B) C3HeB/FeJ pairs were imaged after injection of 2-[^{18}F]-FDG (A) or 2-[^{18}F]-INH (B). Whole-animal sagittal and transverse sections are displayed as combined PET/CT images with heart (H), liver (L), kidneys (K), and bladder (B) marked. Discrete foci of 2-[^{18}F]-INH-PET activity colocalizing with the TB lesions (as seen on CT) is noted in the lung fields of the infected (B) but not the uninfected mouse (A), suggesting that 2-[^{18}F]-INH penetrates and concentrates at the site of TB lesions. Uptake in the heart, liver, kidneys, and bladder is noted in both infected and uninfected animals.

aging, which can evaluate disease processes in live animals, deep within the body, noninvasively and relatively rapidly. An on-table injection and biocontainment system, developed in house, allowed us to determine the real-time pharmacokinetic profile of an ^{18}F analog of INH in *M. tuberculosis*-infected mice. The approach was rapid and noninvasive and visualized the entire animal.

Our data support that similar to INH, 2-F-INH is activated by KatG and accumulates intracellularly in bacteria, but it has reduced activity against InhA. The weaker inhibition of InhA relative to INH may explain the decreased antibacterial activity of 2-F-INH against *M. tuberculosis*. Nevertheless, pathogen-specific enzymatic activation and presumed intracellular trapping make 2-F-INH an interesting candidate as an imaging probe for *M. tuberculosis* and for studying INH pharmacokinetics. By imaging infected and uninfected animals simultaneously, we not only determined organ-specific drug dynamics in challenging compartments like the central nervous system but also noted accumulation of 2-[^{18}F]-INH in the lungs. Diffuse 2-[^{18}F]-INH-PET activity was noted in the lungs of infected BALB/c mice with a signal-to-background ratio of 1.67 at 60 min after tracer injection.

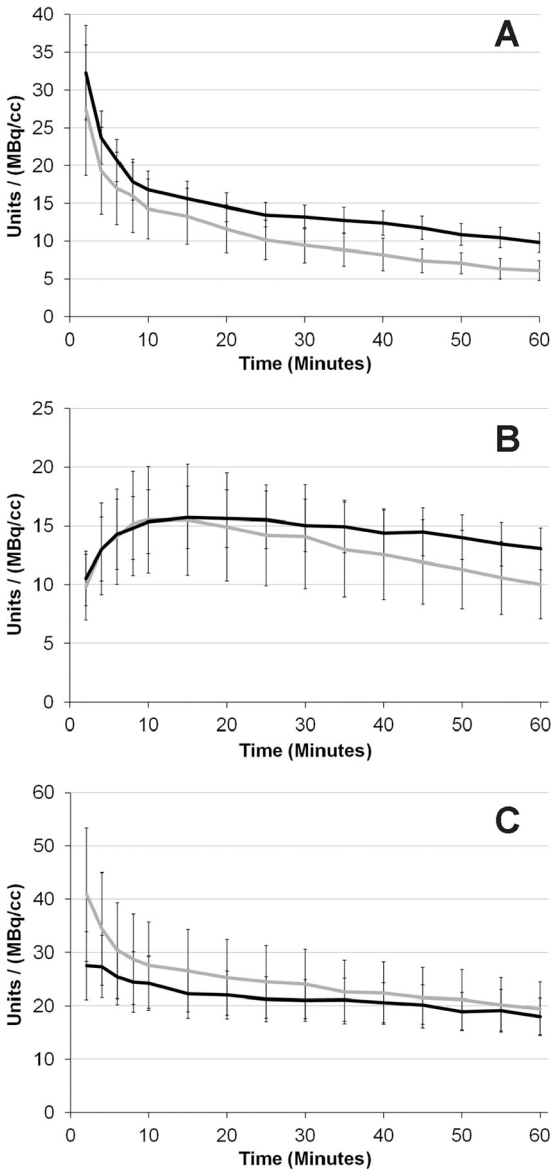

FIG 4 Organ compartment pharmacokinetics of 2-[^{18}F]-INH. Following simultaneous 2-[^{18}F]-INH injections into paired infected and uninfected BALB/c mice, we performed dynamic PET acquisitions over time. There is significantly more 2-[^{18}F]-INH-PET activity in the lung fields (A) of infected mice than in uninfected controls from 40 min postinjection to the end of the recording at 60 min ($P < 0.05$). Uptake of 2-[^{18}F]-INH was evaluated similarly in the brain (B). Probe uptake peaks at 15 min postinjection and then slowly diffuses away. While the signal is greater in infected mice, it is not statistically significant ($P > 0.50$). As expected, the liver intensities are not significantly different ($P > 0.85$) between the infected and uninfected animals (C) but demonstrate high activity, as this is the site of INH metabolism.

This is greater than the 1.32 ratio at 15 min (see Table S1 in the supplemental material) in the lungs, suggesting that these ratios increase with time, presumably due to the selective retention of 2-[^{18}F]-INH in infected tissues and the clearance of the background signal from uninfected tissues. Moreover, discrete foci of PET activity corresponding to the bacterium-rich TB lesions (8) were noted in the lungs of infected C3HeB/FeJ mice. While a nonspecific blood-pooling effect could be contributing in part to the higher PET activity noted in the lungs of infected animals, the similar levels of 2-[^{18}F]-INH PET activity noted in the livers of infected versus uninfected mice argue against this as the dominant phenomena. In our analysis of the brain, we found that 2-[^{18}F]-INH activity peaked 15 min after administration, consistent with the known rapid transit of INH across the blood-brain barrier (20).

We have previously utilized pulmonary [^{18}F]FDG-PET imaging to monitor the response to TB treatments (8). However, [^{18}F]FDG is a nonspecific marker of metabolic activity that relies upon a host inflammatory response. The various *M. tuberculosis* strains produce differing amounts of immune response, with Beijing/W producing significantly more inflammation than Canetti in the BALB/c mouse model of pulmonary infection (21). 2-[^{18}F]-INH therefore would be predicted to be more sensitive than [^{18}F]FDG-PET for diagnosis of the less virulent strains of TB. In addition, [^{18}F]FDG-PET cannot discriminate sterile inflammation from infection (38). By targeting pathogen metabolism rather than the inflammatory response of the host, ^{18}F analogs of INH could be more specific agents for detecting and monitoring TB treatments. Since activated INH binds with a significant residence time to InhA and is presumably trapped within bacteria, increasing the interval between tracer administration and imaging could further increase the signal-to-noise ratio by allowing the washout of the background PET signal. Since the half-life of ^{18}F is only 109 min, use of a longer-lived PET isotope, such as ^{124}I (half-life of 4.2 days), could be used to achieve this goal. Finally, the capacity to differentiate disease by INH-resistant strains would also be a useful corollary of 2-[^{18}F]-INH imaging. Unfortunately this was not tested in the current study, since KatG is a significant virulence factor required for *M. tuberculosis* growth *in vivo* (18), and therefore it would be difficult to generate comparable disease or bacterial burden with the INH-resistant strains in our models. Additional limitations to the probe include relatively high background signal in the liver, heart, and bladder. In the case of disseminated infection, a bacterial signal from these tissues would be obscured with the current shorter half-life of 2-[^{18}F]-INH.

In summary, we validated a fluorinated analog of INH, 2-[^{18}F]-INH, as an imaging probe for determining drug PK in *M. tuberculosis*-infected mice. This approach is rapid and noninvasive, and it can simultaneously visualize multiple compartments. The pathogen-specific metabolism of INH makes it an attractive target for development as an imaging probe. The use of longer-lived positron-emitting isotopes may provide greater signal specificity and allow for development as a TB biomarker. Finally, since PET imaging is extensively used in humans, this technology is applicable for both preclinical and clinical studies with significant potential for translation to other anti-infectives.

ACKNOWLEDGMENTS

This study was funded by the NIH Director's New Innovator Award OD006492 (S.K.J.) and AI084189 (P.J.T).

We thank Eric Nuermberger (JHU) for providing us with the INH-resistant *M. tuberculosis* strains. We also thank Ronnie Mease (JHU) for help with radiosynthesis. Part of this research was carried out at Brookhaven National Laboratory (BNL) under contract DE-AC02-98CH10886 with infrastructure support from its Office of Biological and Environmental Research. We are grateful to Joanna Fowler (BNL) for providing cyclotron and radiosynthesis facilities, Michael Schueller (BNL) for cyclotron operations, and David Alexoff (BNL) and Youwen Xu (BNL) for technical assistance.

REFERENCES

1. **Almeida D, et al.** 2009. Paradoxical effect of isoniazid on the activity of rifampin-pyrazinamide combination in a mouse model of tuberculosis. Antimicrob. Agents Chemother. **53**:4178–4184.
2. **Amartey JK, Al-Jammaz I, Al-Otaibi B, Esguerra C.** 2002. Novel synthesis of 2-[18F]-fluoroisonicotinic acid hydrazide and initial biological evaluation. Nucl. Med. Biol. **29**:817–823.
3. **Banerjee A, et al.** 1994. inhA, a gene encoding a target for isoniazid and ethionamide in Mycobacterium tuberculosis. Science **263**:227–230.
4. **Barre J, Didey F, Delion F, Tillement JP.** 1988. Problems in therapeutic drug monitoring: free drug level monitoring. Ther. Drug Monit. **10**:133–143.
5. **Bass JB, Jr, et al.** 1994. Treatment of tuberculosis and tuberculosis infection in adults and children. American Thoracic Society and The Centers for Disease Control and Prevention. Am. J. Respir. Crit. Care Med. **149**:1359–1374.
6. **Bernstein J, Lott WA, Steinberg BA, Yale HL.** 1952. Chemotherapy of experimental tuberculosis. V. Isonicotinic acid hydrazide (nydrazid) and related compounds. Am. Rev. Tuberc. **65**:357–364.
7. **Davis SL, et al.** 2009. Bacterial thymidine kinase as a noninvasive imaging reporter for Mycobacterium tuberculosis in live animals. PLoS One **4**:e6297. doi:10.1371/journal.pone.0006297.
8. **Davis SL, et al.** 2009. Noninvasive pulmonary [18F]-2-fluoro-deoxy-D-glucose positron emission tomography correlates with bactericidal activity of tuberculosis drug treatment. Antimicrob. Agents Chemother. **53**:4879–4884.
9. **Dickinson JM, Aber VR, Mitchison DA.** 1977. Bactericidal activity of streptomycin, isoniazid, rifampin, ethambutol, and pyrazinamide alone and in combination against Mycobacterium tuberculosis. Am. Rev. Respir. Dis. **116**:627–635.
10. **Dye C, Williams BG.** 2008. Eliminating human tuberculosis in the twenty-first century. J. R. Soc. Interface **5**:653–662.
11. **Eide FF, Gean AD, So YT.** 1993. Clinical and radiographic findings in disseminated tuberculosis of the brain. Neurology **43**:1427–1429.
12. **Fischman AJ, Alpert NM, Babich JW, Rubin RH.** 1997. The role of positron emission tomography in pharmacokinetic analysis. Drug Metab. Rev. **29**:923–956.
13. **Harper J, et al.** 2012. Mouse model of necrotic tuberculosis granulomas develops hypoxic lesions. J. Infect. Dis. **205**:595–602.
14. **Heysell SK, Moore JL, Keller SJ, Houpt ER.** 2010. Therapeutic drug monitoring for slow response to tuberculosis treatment in a state control program, Virginia, U. S. A. Emerg. Infect. Dis. **16**:1546–1553.
15. **Hooker JM.** 2010. Modular strategies for PET imaging agents. Curr. Opin. Chem. Biol. **14**:105–111.
16. **Jenne JW, Beggs WH.** 1973. Correlation of in vitro and in vivo kinetics with clinical use of isoniazid, ethambutol, and rifampin. Am. Rev. Respir. Dis. **107**:1013–1021.
17. **Langer O, Muller M.** 2004. Methods to assess tissue-specific distribution and metabolism of drugs. Curr. Drug Metab. **5**:463–481.
18. **Li Z, Kelley C, Collins F, Rouse D, Morris S.** 1998. Expression of katG in Mycobacterium tuberculosis is associated with its growth and persistence in mice and guinea pigs. J. Infect. Dis. **177**:1030–1035.
19. **Lillebaek T, et al.** 2002. Molecular evidence of endogenous reactivation of Mycobacterium tuberculosis after 33 years of latent infection. J. Infect. Dis. **185**:401–404.
20. **Liu L, et al.** 2010. Radiosynthesis and bioimaging of the tuberculosis chemotherapeutics isoniazid, rifampicin and pyrazinamide in baboons. J. Med. Chem. **53**:2882–2891.
21. **Lopez B, et al.** 2003. A marked difference in pathogenesis and immune response induced by different Mycobacterium tuberculosis genotypes. Clin. Exp. Immunol. **133**:30–37.
22. **Lu H, Tonge PJ.** 2010. Drug-target residence time: critical information for lead optimization. Curr. Opin. Chem. Biol. **14**:467–474.
23. **Luckner SR, Liu N, am Ende CW, Tonge PJ, Kisker C.** 2010. A slow, tight binding inhibitor of InhA, the enoyl-acyl carrier protein reductase from Mycobacterium tuberculosis. J. Biol. Chem. **285**:14330–14337.
24. **McKenzie C.** 2011. Antibiotic dosing in critical illness. J. Antimicrob. Chemother. **66**(Suppl. 2):ii25–ii31.
25. **Miller PW, Long NJ, Vilar R, Gee AD.** 2008. Synthesis of 11C, 18F, 15O, and 13N radiolabels for positron emission tomography. Angew. Chem. Int. Ed. Engl. **47**:8998–9033.
26. **Muller M, dela Pena A, Derendorf H.** 2004. Issues in pharmacokinetics and pharmacodynamics of anti-infective agents: distribution in tissue. Antimicrob. Agents Chemother. **48**:1441–1453.
27. **Musser JM, et al.** 1996. Characterization of the catalase-peroxidase gene (katG) and inhA locus in isoniazid-resistant and -susceptible strains of Mycobacterium tuberculosis by automated DNA sequencing: restricted array of mutations associated with drug resistance. J. Infect. Dis. **173**:196–202.
28. **Pan H, et al.** 2005. Ipr1 gene mediates innate immunity to tuberculosis. Nature **434**:767–772.
29. **Parikh S, Moynihan DP, Xiao G, Tonge PJ.** 1999. Roles of tyrosine 158 and lysine 165 in the catalytic mechanism of InhA, the enoyl-ACP reductase from Mycobacterium tuberculosis. Biochemistry **38**:13623–13634.
30. **Parkin DP, et al.** 1997. Trimodality of isoniazid elimination: phenotype and genotype in patients with tuberculosis. Am. J. Respir. Crit. Care Med. **155**:1717–1722.
31. **Pasipanodya JG, Srivastava S, Gumbo T.** 2012. Meta-analysis of clinical studies supports the pharmacokinetic variability hypothesis for acquired drug resistance and failure of antituberculosis therapy. Clin. Infect. Dis. **55**:169–177.
32. **Prideaux B, et al.** 2011. High-sensitivity MALDI-MRM-MS imaging of moxifloxacin distribution in tuberculosis-infected rabbit lungs and granulomatous lesions. Anal. Chem. **83**:2112–2118.
33. **Rawat R, Whitty A, Tonge PJ.** 2003. The isoniazid-NAD adduct is a slow, tight-binding inhibitor of InhA, the Mycobacterium tuberculosis enoyl reductase: adduct affinity and drug resistance. Proc. Natl. Acad. Sci. U. S. A. **100**:13881–13886.
34. **Rouse DA, DeVito JA, Li Z, Byer H, Morris SL.** 1996. Site-directed mutagenesis of the katG gene of Mycobacterium tuberculosis: effects on catalase-peroxidase activities and isoniazid resistance. Mol. Microbiol. **22**:583–592.
35. **Sato T, et al.** 2009. Discovery of 3-(2-cyano-4-pyridyl)-5-(4-pyridyl)-1,2,4-triazole, FYX-051, a xanthine oxidoreductase inhibitor for the treatment of hyperuricemia. Bioorg. Med. Chem. Lett. **19**:6225–6229.
36. **Schaaf HS, et al.** 2005. Isoniazid pharmacokinetics in children treated for respiratory tuberculosis. Arch. Dis. Child. **90**:614–618.
37. **Schmidt S, Banks R, Kumar V, Rand KH, Derendorf H.** 2008. Clinical microdialysis in skin and soft tissues: an update. J. Clin. Pharmacol. **48**:351–364.
38. **Signore A, Glaudemans AW.** 2011. The molecular imaging approach to image infections and inflammation by nuclear medicine techniques. Ann. Nucl. Med. **25**:681–700.
39. **Timmins GS, Deretic V.** 2006. Mechanisms of action of isoniazid. Mol. Microbiol. **62**:1220–1227.
40. **Weber WW, Hein DW.** 1979. Clinical pharmacokinetics of isoniazid. Clin. Pharmacokinet. **4**:401–422.
41. **World Health Organization.** 2011. Global tuberculosis control 2011. World Health Organization, Geneva, Switzerland.
42. **Zhang Y, Heym B, Allen B, Young D, Cole S.** 1992. The catalase-peroxidase gene and isoniazid resistance of Mycobacterium tuberculosis. Nature **358**:591–593.
43. **Zhao X, et al.** 2006. Hydrogen peroxide-mediated isoniazid activation catalyzed by Mycobacterium tuberculosis catalase-peroxidase (KatG) and its S315T mutant. Biochemistry **45**:4131–4140.

AAC
Journals.ASM.org

ERRATUM

Noninvasive Determination of 2-[^{18}F]-Fluoroisonicotinic Acid Hydrazide Pharmacokinetics by Positron Emission Tomography in *Mycobacterium tuberculosis*-Infected Mice

E. A. Weinstein, L. Liu, A. A. Ordonez, H. Wang, J. M. Hooker, P. J. Tonge, S. K. Jain

Center for Infection and Inflammation Imaging, Center for Tuberculosis Research, Department of Medicine, and Department of Pediatrics, Johns Hopkins University School of Medicine, Baltimore, Maryland, USA; Institute for Chemical Biology & Drug Discovery, Department of Chemistry, Stony Brook University, Stony Brook, New York, USA; Martinos Center for Biomedical Imaging, Massachusetts General Hospital and Harvard Medical School, Charlestown, Massachusetts, USA

Volume 56, no. 12, p. 6284–6290, 2012. Page 6288: Figure 3 legend, lines 1 and 2, "Uninfected (A) and infected (B) C3HeB/FeJ pairs were imaged after injection of 2-[^{18}F]-FDG (A) or 2-[^{18}F]-INH (B)" should read "Uninfected (A) and infected (B) C3HeB/FeJ pairs were imaged after injection of 2-[^{18}F]-INH."

doi:10.1128/AAC.02274-12